Angular distributions of Drell-Yan lepton pairs at the Fermilab Tevatron: Order α_s^2 corrections and Monte Carlo studies

E. Mirkes

Department of Physics, University of Wisconsin, Madison, Wisconsin 53706

J. Ohnemus

Department of Physics, University of California, Davis, California 95616
(Received 13 December 1994)

We investigate the angular distribution of the lepton pair in the process $p\bar{p} \to \gamma^* + X \to \ell^+\ell^- + X$, where the virtual photon is produced at high transverse momentum. The angular distribution of the leptons is very sensitive to possible nonperturbative effects, such as a nontrivial vacuum structure of QCD, and offers a good chance to test such effects. We present complete $O(\alpha_s^2)$ calculations of the decay lepton distributions in the lepton pair rest frame. An order $O(\alpha_s)$ Monte Carlo study of the lepton angular distributions, with acceptance cuts and energy resolution smearing applied to the leptons, is also presented.

PACS number(s): 13.85.Qk, 12.38.Bx

I. INTRODUCTION

The production of a virtual photon at hadron colliders, along with the subsequent decay into a lepton pair, provides a unique opportunity for testing perturbative quantum chromodynamics (QCD). In particular, the measurement of the angular distribution of the decay leptons provides a detailed test of the production mechanism of the virtual photon. Experimental studies of the angular distribution of the lepton pair have been made by the NA10 collaboration at CERN [1] and the Chicago-Iowa-Princeton collaboration at Fermilab [2]. The data from these experiments do not agree with the predictions of the QCD improved parton model. An investigation of the decay lepton distribution at the Fermilab Tevatron center of mass energy would certainly be interesting in view of these results. In this paper, we present next-to-leading-order QCD predictions for the angular distributions of the lepton pair in the process $p\bar{p} \to \gamma^* + X \to \ell^+\ell^- + X$ at Tevatron energies together with a leading-order Monte Carlo study in which acceptance cuts and energy resolution smearing are applied to the leptons.

A basic assumption in the calculation of the Drell-Yan process [3] is the factorization hypothesis, which asserts that the hadronic cross section can be calculated by convoluting the cross section for the corresponding parton level reaction, $q\bar{q} \to \gamma^* \to \ell^+\ell^-$, with the parton distribution functions of the initial state hadrons. Great theoretical efforts have been made to prove this factorization assumption within perturbative QCD [4]. However, in Ref. [5] it has been argued that nonperturbative QCD effects may spoil the factorization. Nonperturbative vacuum fluctuations could generate a background field (such as the color domains described in the first paper of Ref. [5]) which could induce spin and color correlations between the partons of the incoming hadrons. These effects need *not* vanish in the high energy limit, i.e., they can be "leading twist" effects (for reviews see

Ref. [6]).

It has recently been shown [7] that the decay lepton distribution of a vector boson produced in hadronic collisions is very sensitive to nonperturbative effects and offers a good chance to test the factorization hypothesis. As mentioned earlier, the experimental results in Refs. [1] and [2] for the decay lepton distribution from a virtual photon produced in pion-nucleon scattering are not in agreement with next-to-leading-order QCD predictions [7] and therefore give an indication that factorization may be violated. In Ref. [7], it has been shown that these results can be explained by transverse spin correlations between the initial state partons, which may be induced by the nontrivial vacuum structure in QCD. Pion bound state effects have been discussed in Ref. [8] as another possible explanation for the discrepancy.

It would clearly be interesting to check whether the decay lepton distributions from gauge bosons produced at the Tevatron are in agreement with the factorization assumption. To do this test, reliable theoretical predictions for the decay distributions are mandatory. In this paper, we present complete next-to-leading-order $[O(\alpha_s^2)]$ predictions for the angular distributions of the leptons produced via the decay of a high p_T virtual photon, i.e., the Drell-Yan process $p\bar{p} \to \gamma^* + X \to \ell^+\ell^- + X$ is calculated to $O(\alpha_s^2)$. The calculation is based on the assumption of factorization, i.e., the calculation is done in the standard QCD-improved parton model. When the virtual photon is produced with no transverse momentum, the zero order Drell-Yan subprocess, $q\bar{q} \to \gamma^* \to \ell^+\ell^-$, predicts a $1 + \cos^2\theta$ distribution for the leptons, where θ is the scattering angle in the parton center of mass frame (the γ^* rest frame). For virtual photons produced with transverse momentum (balanced by additional gluons or quarks), the event plane spanned by the beam and virtual photon momentum directions provides a convenient reference plane for studying the angular distributions of the decay leptons. The angular distribution now has the general form

$$\frac{d\sigma}{d\phi\, d\cos\theta} \sim (1 + \cos\theta^2) + \frac{1}{2}\, A_0\, (1 - 3\cos^2\theta)$$

$$+ A_1\, \sin 2\theta \cos\phi + \frac{1}{2}\, A_2\, \sin^2\theta \cos 2\phi\,, \quad (1)$$

where θ and ϕ denote the polar and azimuthal angles of the decay leptons in the virtual photon rest frame. The coefficients A_i are functions of the transverse momentum and rapidity of the virtual photon (measured in the laboratory frame) and vanish in the limit $p_T(\gamma^*) \to 0$.

The remainder of this paper is organized as follows. In Sec. II we discuss the formalism for describing the angular distributions of the decay leptons, give an overview of the $O(\alpha_s^2)$ calculation of the process $p\bar{p} \to \gamma^* + X \to \ell^+\ell^- + X$, and define two choices for the z axis in the lepton pair rest frame. In Sec. III we present $O(\alpha_s^2)$ numerical results for the coefficients A_i and show that the QCD corrections to the coefficients are fairly small. This is because the coefficients A_i are ratios of helicity cross sections [see Eq. (11)] and the QCD corrections tend to cancel in these ratios. A leading-order $[O(\alpha_s)]$ Monte Carlo study of the decay lepton distributions for the Tevatron center of mass energy, with typical acceptance cuts and energy resolution smearing applied to the leptons, is also given. Conclusions and summary are given in Sec. IV. Finally, there is an Appendix containing next-to-leading-order matrix elements which contribute to virtual photon production but have not appeared in the literature.

II. FORMALISM

The formalism used in our calculations is discussed in this section. First, the methodology for describing the angular distributions of the leptons is reviewed, then an overview of the $O(\alpha_s^2)$ calculation of the process $p\bar{p} \to \gamma^* + X \to \ell^+\ell^- + X$ is given, and finally, two choices for the z axis in the lepton pair rest frame are defined.

A. Angular distributions

We consider the angular distributions of the leptons coming from the leptonic decay of a virtual photon produced with nonzero transverse momentum in high energy proton-antiproton collisions. For definiteness we take

$$p(P_1) + \bar{p}(P_2) \to \gamma^*(Q) + X \to \ell^+(\ell_1) + \ell^-(\ell_2) + X\,, \quad (2)$$

where the quantities in parentheses denote the four-momenta of the particles. At leading order $[O(\alpha_s)]$ the parton subprocesses,

$$q + \bar{q} \to \gamma^* + g\,, \quad q + g \to \gamma^* + q\,, \quad (3)$$

contribute to high p_T virtual photon production.

In the parton model the hadronic cross section is obtained by folding the hard scattering parton level cross section with the respective parton densities:

$$\frac{d\sigma^{h_1 h_2}}{dQ^2\, dp_T^2\, dy\, d\Omega^*} = \sum_{a,b} \int dx_1\, dx_2\, f_a^{h_1}(x_1, \mu_F^2)\, f_b^{h_2}(x_2, \mu_F^2)\, \frac{s\, d\hat{\sigma}_{ab}}{dQ^2\, dt\, du\, d\Omega^*}\, (x_1 P_1, x_2 P_2, \alpha_s(\mu_R^2))\,, \quad (4)$$

where the sum is over $a, b = q, \bar{q}, g$. $f_a^h(x, \mu_F^2)$ is the probability density for finding parton a with momentum fraction x in hadron h when it is probed at scale μ_F^2. The parton level cross section for the subprocesses in Eq. (3) are denoted by $d\hat{\sigma}_{ab}$. Note that in the framework of the parton model the incoming partons are assumed to be unpolarized in spin and color (for unpolarized initial state hadrons). Furthermore, one neglects the transverse momenta of the incoming partons. (This is in contrast to the model discussed in Ref. [7], where it is assumed that a nontrivial structure of the QCD vacuum correlates the spins and momenta of the incoming partons. Given such a correlation, it has been shown that these correlations can drastically affect the polarization of the produced boson [7].)

Denoting hadron level and parton level quantities by upper and lower case characters, respectively, the hadron and parton level Mandelstam variables are defined by

$$S = (P_1 + P_2)^2\,, \quad T = (P_1 - Q)^2\,, \quad U = (P_2 - Q)^2\,, \quad (5)$$

and

$$\begin{aligned}
s &= (p_1 + p_2)^2 &&= x_1 x_2 S\,, \\
t &= (p_1 - Q)^2 &&= x_1(T - Q^2) + Q^2\,, \\
u &= (p_2 - Q)^2 &&= x_2(U - Q^2) + Q^2\,,
\end{aligned} \quad (6)$$

where $p_1 = x_1 P_1$ and $p_2 = x_2 P_2$. The rapidity y of the virtual photon in the laboratory frame can be written

$$y = \frac{1}{2}\ln\left(\frac{Q^2 - U}{Q^2 - T}\right)\,, \quad (7)$$

and the transverse momentum p_T of the virtual photon is related to the Mandelstam variables via

$$p_T^2 = \frac{(Q^2 - U)(Q^2 - T)}{S} - Q^2\,. \quad (8)$$

The angles θ and ϕ in $d\Omega^* = d\cos\theta\, d\phi$ are the polar and azimuthal decay angles of the leptons in the virtual photon rest frame, measured with respect to a coordinate system to be described later. The angular dependence of the differential cross section in Eq. (4) can be written (see Ref. [9] for details)

$$\frac{16\pi}{3}\frac{d\sigma}{dQ^2\, dp_T^2\, dy\, d\cos\theta\, d\phi} = \frac{d\sigma^{U+L}}{dQ^2\, dp_T^2\, dy}(1 + \cos^2\theta) + \frac{d\sigma^L}{dQ^2\, dp_T^2\, dy}(1 - 3\cos^2\theta) \quad (9)$$

$$+ \frac{d\sigma^T}{dQ^2\, dp_T^2\, dy}\, 2\sin^2\theta \cos 2\phi + \frac{d\sigma^I}{dQ^2\, dp_T^2\, dy}\, 2\sqrt{2}\sin 2\theta \cos\phi\,.$$

The unpolarized differential production cross section is denoted by σ^{U+L} whereas $\sigma^{L,T,I}$ characterize the polarization of the virtual photon, e.g., the cross section for longitudinally polarized virtual photons is denoted by σ^L, the transverse interference cross section by σ^T, and the transverse-longitudinal interference cross section by σ^I (all with respect to the chosen z axis of the lepton pair rest frame). The hadronic helicity cross sections $\frac{d\sigma^\alpha}{dQ^2\,dp_T^2\,dy}$ in Eq. (9) are obtained by convoluting the partonic helicity cross sections with the parton densities:

$$\frac{d\sigma^\alpha}{dQ^2\,dp_T^2\,dy} = \int\,dx_1\,dx_2\,f^{h_1}(x_1,\mu_F^2)\,f^{h_2}(x_2,\mu_F^2)\,\frac{s\,d\hat\sigma^\alpha}{dQ^2\,dt\,du}\,. \tag{10}$$

Introducing the standard angular coefficients [10]

$$A_0 = \frac{2\,d\sigma^L}{d\sigma^{U+L}}\,, \qquad A_1 = \frac{2\sqrt{2}\,d\sigma^I}{d\sigma^{U+L}}\,, \qquad A_2 = \frac{4\,d\sigma^T}{d\sigma^{U+L}}\,, \tag{11}$$

the angular distribution in Eq. (9) can be conveniently written

$$\frac{d\sigma}{dQ^2\,dp_T^2\,dy\,d\cos\theta\,d\phi} = \frac{3}{16\pi}\frac{d\sigma^{U+L}}{dQ^2\,dp_T^2\,dy}\left[(1+\cos^2\theta)+\frac{1}{2}A_0(1-3\cos^2\theta)\right. \tag{12}$$

$$\left. +A_1\sin 2\theta\cos\phi+\frac{1}{2}A_2\sin^2\theta\cos 2\phi\right]\,.$$

Integrating the angular distribution in Eq. (12) over the azimuthal angle ϕ yields

$$\frac{d\sigma}{dQ^2\,dp_T^2\,dy\,d\cos\theta} = C\,(1+\alpha\cos^2\theta)\,, \tag{13}$$

where

$$C = \frac{3}{8}\frac{d\sigma^{U+L}}{dQ^2\,dp_T^2\,dy}\left[1+\frac{A_0}{2}\right]\,, \qquad \alpha = \frac{2-3A_0}{2+A_0}\,. \tag{14}$$

Integrating Eq. (12) over the polar angle θ yields

$$\frac{d\sigma}{dQ^2\,dp_T^2\,dy\,d\phi} = \frac{1}{2\pi}\frac{d\sigma^{U+L}}{dQ^2\,dp_T^2\,dy}\,(1+\beta\cos 2\phi)\,, \tag{15}$$

where

$$\beta = \frac{A_2}{4}\,. \tag{16}$$

By taking moments with respect to an appropriate product of trigonometric functions it is possible to disentangle the coefficients A_i. A convenient definition of the moments is [11]

$$\langle m\rangle = \frac{\int d\sigma(p_T,y,\theta,\phi)\,m\,d\cos\theta\,d\phi}{\int d\sigma(p_T,y,\theta,\phi)\,d\cos\theta\,d\phi}\,, \tag{17}$$

which leads to the following results:

$$\langle 1\rangle = 1\,, \tag{18}$$

$$\left\langle\frac{1}{2}(1-3\cos^2\theta)\right\rangle = \frac{3}{20}\left(A_0-\frac{2}{3}\right)\,, \tag{19}$$

$$\langle\sin 2\theta\cos\phi\rangle = \frac{1}{5}A_1\,, \tag{20}$$

$$\langle\sin^2\theta\cos 2\phi\rangle = \frac{1}{10}A_2\,. \tag{21}$$

B. Next-to-leading-order cross section

At $O(\alpha_s^2)$ the following partonic tree level and one-loop processes contribute to the partonic helicity cross sections $\frac{s\,d\hat\sigma^\alpha}{dQ^2\,dt\,du}$ in Eq. (10):

$$\text{tree level contributions}: \begin{array}{l} q+\bar q \rightarrow \gamma^*+g+g\,, \\ q+\bar q \rightarrow \gamma^*+q+\bar q\,, \\ q+g \rightarrow \gamma^*+q+g\,, \\ q+q \rightarrow \gamma^*+q+q\,, \\ g+g \rightarrow \gamma^*+q+\bar q\,, \end{array} \tag{22}$$

$$\text{one-loop contributions}: \begin{array}{l} q+\bar q \rightarrow \gamma^*+g\,, \\ q+g \rightarrow \gamma^*+q\,. \end{array} \tag{23}$$

The second-order contributions in Eq. (23) come from the interference of the one-loop diagrams with the leading-order diagrams. Let us briefly sketch the technical ingredients that go into our calculation (for more details, see Ref. [9]). For the $O(\alpha_s^2)$ tree level contributions in Eq. (22) we introduce the variable

$$s_2 = (k_1+k_2)^2 = (p_1+p_2-Q)^2 = s+t+u-Q^2\,, \tag{24}$$

in addition to s,t,u defined in Eq. (6); s_2 is the invariant mass of the system recoiling against the virtual photon.

To obtain the p_T distribution of the virtual photon, the $O(\alpha_s^2)$ tree level diagrams must to be integrated over the phase space of the two final state partons with the p_T of the virtual photon held fixed. The integration over the recoiling partons is most easily performed in the (k_1k_2) center of mass system by integrating over the solid angle $d\Omega_{k_1k_2}$. Since all partons are massless, collinear divergencies appear after integrating over $d\Omega_{k_1k_2}$. Soft gluon singularities show up as poles in the variable s_2. A finite next-to-leading-order (NLO) partonic helicity cross

section is derived in the following manner. Infrared and collinear divergencies associated with final state partons cancel among loop and tree diagrams. Collinear initial state divergencies are absorbed into the parton densities, i.e., they are removed by renormalizing the parton densities, which introduces a factorization scale dependence into the parton densities $f(x, \mu_F^2)$. Ultraviolet divergencies are removed by $\overline{\mathrm{MS}}$ (modified minimal subtraction [12]) renormalization, which introduces a renormalization scale dependence into the strong coupling constant $\alpha_s(\mu_R^2)$.

Following Ref. [9], we introduce the following notation to list the partonic helicity cross sections $\frac{s\,d\hat{\sigma}_{ab}^\alpha}{dQ^2\,dt\,du}$ in Eq. (10) $[\alpha \in \{U + L, L, T, I\}]$.

$O(\alpha_s)$ Born contributions:

$$\frac{s\,d\hat{\sigma}_{ab}^{\alpha,\mathrm{Born}}}{dQ^2\,dt\,du} = \frac{K_{ab}^{\gamma^*}}{s}\,\alpha_s\,\delta(s + t + u - Q^2)\,T_{ab}^\alpha(B)\,, \quad (25)$$

$O(\alpha_s^2)$ virtual corrections:

$$\frac{s\,d\hat{\sigma}_{ab}^{\alpha,\mathrm{virt}}}{dQ^2\,dt\,du} = \frac{K_{ab}^{\gamma^*}}{s}\,\frac{\alpha_s^2}{2\pi}\,\delta(s + t + u - Q^2)\,V(\varepsilon)\,T_{ab}^\alpha(V)\,, \quad (26)$$

$O(\alpha_s^2)$ tree graph corrections:

$$\frac{s\,d\hat{\sigma}_{ab}^{\alpha,\mathrm{tree}}}{dQ^2\,dt\,du} = \frac{K_{ab}^{\gamma^*}}{s}\,\frac{\alpha_s^2}{2\pi}\,V(\varepsilon)\,T_{ab}^\alpha(T)\,. \quad (27)$$

The subscript ab stands for the initial state parton pair, i.e., a and b denote a quark, antiquark, or gluon. The initial state collinear singularities have been factorized from Eq. (27) at a scale μ_F^2. The constants $K_{ab}^{\gamma^*}$ and $V(\varepsilon)$ are given by (we work in $n = 4 - 2\varepsilon$ dimensions)

$$K_{qq}^{\gamma^*} = \frac{16\pi}{3}\,\frac{\alpha^2}{8\pi Q^2}\,\frac{C_F}{N_C}\,\frac{(1 - \varepsilon)}{\Gamma(1 - \varepsilon)}\left(\frac{4\pi\mu^2}{Q^2}\right)^\varepsilon\left(\frac{sQ^2}{ut}\right)^\varepsilon\,, \quad (28)$$

$$K_{qg}^{\gamma^*} = \frac{K_{qq}^{\gamma^*}}{2\,C_F\,(1 - \varepsilon)}\,, \quad (29)$$

$$K_{gg}^{\gamma^*} = \frac{K_{qq}^{\gamma^*}}{4C_F^2\,(1 - \varepsilon)^2}\,, \quad (30)$$

$$V(\varepsilon) = \frac{\Gamma(1 - \varepsilon)}{\Gamma(1 - 2\varepsilon)}\left(\frac{4\pi\mu^2}{Q^2}\right)^\varepsilon\,. \quad (31)$$

$T_{ab}^\alpha(B, V, T)$ are the partonic helicity matrix elements for the Born, virtual, and tree contributions. The explicit form of the partonic helicity matrix elements depends on the choice of the z axis in the γ^* rest frame. Covariant projection cross sections $d\hat{\sigma}^\beta$ $[\beta \in \{U + L, L_1, L_2, L_{12}\}]$ for W boson production have been calculated to $O(\alpha_s^2)$ in Ref. [9]. From these results one can obtain the relevant helicity cross sections in Eqs. (25)–(27) for any given γ^* rest frame [see Eqs. (A1) and (A3)]. However, there are some further contributions in the case of γ^* production, which do not contribute to W boson production because of charge conservation. The diagrams can be found in Figs. 8 and 9 of Ref. [9]. The remaining analyt-

ical projections for these contributions (after integration over $d\Omega_{k_1 k_2}$) are listed here in an Appendix. The folding of the NLO parton level cross sections with the respective parton densities is straightforward, and we do not list the combinations here.

C. The z axis in the lepton pair rest frame

Before we present numerical results for the angular distributions, it is necessary to discuss the choice of the z axis in the lepton-pair rest frame. We will discuss two different choices: the Collins-Soper (CS) frame [10] and the Gottfried-Jackson (GJ) frame [13]. In the CS frame the z axis bisects the angle between $\vec{P}_1$ and $-\vec{P}_2$:

$$\vec{P}_1 = E_1\,(\sin\gamma_{\mathrm{CS}}, 0, \cos\gamma_{\mathrm{CS}})\,,$$
$$\vec{P}_2 = E_2\,(\sin\gamma_{\mathrm{CS}}, 0, -\cos\gamma_{\mathrm{CS}})\,, \quad (32)$$

with

$$\cos\gamma_{\mathrm{CS}} = \left(\frac{Q^2 S}{(T - Q^2)(U - Q^2)}\right)^{1/2} = \left(\frac{Q^2}{Q^2 + p_T^2}\right)^{1/2}\,, \quad (33)$$

$$\sin\gamma_{\mathrm{CS}} = -\sqrt{1 - \cos^2\gamma_{\mathrm{CS}}}\,, \quad (34)$$

$$E_1 = \frac{Q^2 - T}{2\sqrt{Q^2}}\,, \qquad E_2 = \frac{Q^2 - U}{2\sqrt{Q^2}}\,. \quad (35)$$

In the GJ frame the z axis is chosen parallel to the beam axis:

$$\vec{P}_1 = E_1\,(0, 0, 1)\,,$$
$$\vec{P}_2 = E_2\,(\sin\gamma_{\mathrm{GJ}}, 0, \cos\gamma_{\mathrm{GJ}})\,, \quad (36)$$

with

$$\cos\gamma_{\mathrm{GJ}} = 1 - \frac{2Q^2 S}{(T - Q^2)(U - Q^2)} = \frac{p_T^2 - Q^2}{p_T^2 + Q^2}\,, \quad (37)$$

$$\sin\gamma_{\mathrm{GJ}} = -\sqrt{1 - \cos^2\gamma_{\mathrm{GJ}}}\,, \quad (38)$$

$$E_1 = \frac{Q^2 - T}{2Q}\,, \qquad E_2 = \frac{Q^2 - U}{2Q}\,. \quad (39)$$

Note that the CS and GJ frames are related by a rotation about the y axis. In the laboratory frame, the z direction is defined by the proton momentum and the x direction is defined by the transverse momentum of the virtual photon.

III. NUMERICAL RESULTS

In this section numerical results are presented for high p_T production and leptonic decay of a virtual photon at the Tevatron collider center of mass energy ($\sqrt{S} = 1.8$ TeV). The numerical results have been obtained using the Martin-Roberts-Stirling (MRS) set A [14] parton distribution functions with $\Lambda_{\overline{\mathrm{MS}}}^{(4)} = 230$ MeV. For our NLO predictions, we use the two-loop formula for α_s with five flavors. If not stated otherwise, the renormalization scale

μ_R^2 and the factorization scale μ_F^2 in Eq. (4) have been taken to be $\mu_R^2 = \mu_F^2 = [Q^2 + p_T^2(\gamma^*)]/2$, where Q and $p_T(\gamma^*)$ are the invariant mass and transverse momentum, respectively, of the virtual photon. We work in the $\overline{\text{MS}}$ factorization scheme.

We begin with numerical results for the coefficients A_i, α, and β in Eqs. (12), (13), and (15). Figure 1(a) shows the coefficients A_0, A_1, and A_2 in the CS frame as functions of $p_T(\gamma^*)$ for an invariant mass Q of the photon fixed to $Q = 10$ GeV. The reason for choosing this fairly large invariant mass is to minimize the effect of the acceptance cuts which will later be imposed on the decay leptons (see below). The dotted lines are leading order (LO) $[O(\alpha_s^1)]$ predictions and the solid lines are next-to-leading-order $[O(\alpha_s^2)]$ predictions. The coefficients A_0 and A_2 are increasing functions of $p_T(\gamma^*)$ and the deviations from the zero order $[O(\alpha_s^0)]$ expectation $[A_0 = A_2 = 0$ at $p_T(\gamma^*) = 0]$ are quite large, even at modest values of $p_T(\gamma^*)$. It has been noted in Ref. [15] that the coefficients A_0 and A_2 are exactly equal at LO (dotted line). This is no longer true at NLO, but the corrections are fairly small, especially the corrections to A_0. The $O(\alpha_s^2)$ corrections to A_2 are negative and about 20% the size of the LO result. Note that A_0 originates from the longitudinal polarization of the virtual photon, whereas A_2 receives contributions from a transversely polarized virtual photon (all with respect to the z axis of the chosen lepton-pair rest frame). The deviation of A_1 (interference of longitudinal and transverse virtual photon polarizations) from zero is small in the CS frame, even at large values of $p_T(\gamma^*)$.

Figure 1(b) shows numerical results for the coefficients α and β [see Eqs. (13) and (15)] as a function of $p_T(\gamma^*)$. The coefficients are again very sensitive to the transverse momentum of the virtual photon, and the deviations from the zero order predictions ($\alpha = 1$ and $\beta = 0$)

are again large. The NLO corrections to α are small over the whole range of $p_T(\gamma^*)$.

Numerical results for the coefficients A_i, α, and β in the GJ frame are shown in Fig. 2. The corrections to A_0 and α are larger than in the CS frame, however, in both frames the corrections do not dramatically change the LO results. This is because the coefficients A_i are ratios of helicity cross sections [see Eq. (11)], and the large QCD corrections in the individual helicity cross sections tend to cancel in the ratios. This can be seen from Fig. 3, where the K factors for the helicity cross sections σ^{U+L}, σ^L, and σ^T are shown as functions of $p_T(\gamma^*)$ in the CS frame [Fig. 3(a)] and GJ frame [Fig. 3(b)]. The K factor is defined as the ratio of the NLO $[O(\alpha_s^2)]$ differential cross section to the LO $[O(\alpha_s^1)]$ differential cross section. Results are shown in Fig. 3 for two different choices of the scale $\mu^2 = \mu_F^2 = \mu_R^2$: the upper curves correspond to $\mu^2 = 1/4 [p_T^2(\gamma^*) + Q^2]$ and the lower curves correspond to $\mu^2 = 4 [p_T^2(\gamma^*) + Q^2]$. The invariant mass of the virtual photon has again been fixed to $Q = 10$ GeV. The K factor for σ^{U+L} and σ^L ranges from 0.9 to 1.6 in the CS frame depending on $p_T(\gamma^*)$ and the choice of the renormalization and factorization scale. However, the K-factor is almost the same for σ^{U+L} and σ^L, thus A_0, which is proportional to the ratio σ^L/σ^{U+L}, is not effected by the corrections. In the GJ frame, the K factors for σ^L and σ^{U+L} differ more, and thus the corrections to A_0 are larger in the GJ frame [see Fig. 2(b)]. The K factors for σ^T are particularly different from the K factors for σ^{U+L}, which explains the large deviation of A_2 from the LO result $A_0 = A_2$. Note that the large K factors are due to large logarithms [like $\ln(s/Q^2)$] in the NLO matrix elements [9]. The K factors decrease with increasing invariant mass of the virtual photon.

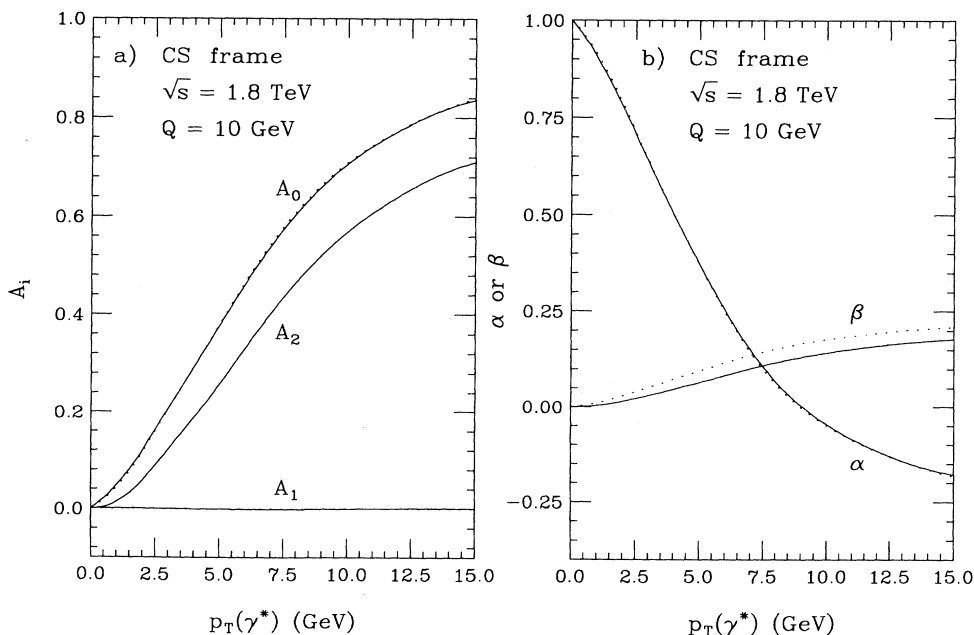To give a feeling for the numerical contributions from the different partonic subprocesses, Fig. 4 shows the

FIG. 1. Angular coefficients for γ^* production and decay in the CS frame as a function of the transverse momentum $p_T(\gamma^*)$ for $Q = 10$ GeV and $\sqrt{S} = 1.8$ TeV. Part (a) shows the angular coefficients A_0, A_1, and A_2 and part (b) shows the angular coefficients α and β. The dotted lines are LO predictions ($A_0 = A_2$ at LO) and the solid lines are NLO predictions. No cuts or smearing have been applied.

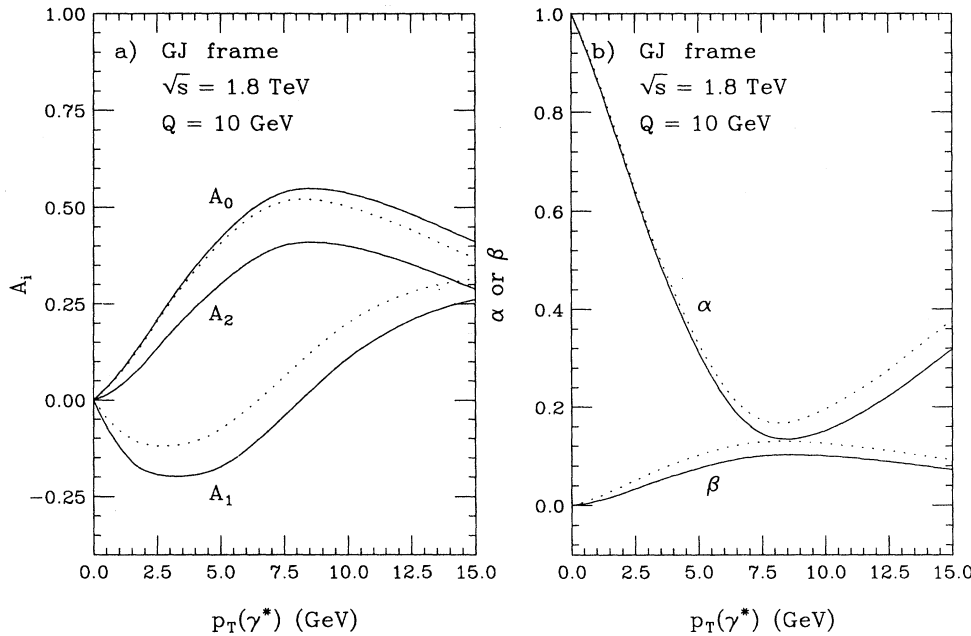FIG. 2. Same as Fig. 1 but for the GJ frame.

fractional contributions of the partonic subprocesses to σ^{U+L}, σ^L, and σ^T for γ^* production as a function of $p_T(\gamma^*)$ for $Q = 10$ GeV. The curves labeled A and B correspond to the LO results from the subprocesses $q\bar{q} \to \gamma^* g$ and $qg \to \gamma^* q$, respectively. The curves labeled C through G correspond to the $O(\alpha_s^2)$ contributions from the subprocesses listed in Eqs. (22) and (23). Note that the NLO contribution from the qg initiated subprocess (curve E) is more important than the LO contribution from the $q\bar{q}$ subprocess (curve A) at large values of $p_T(\gamma^*)$. The other $O(\alpha_s^2)$ subprocesses are fairly small

and even give negative contributions at small values of $p_T(\gamma^*)$. This is due to the factorization of the collinear initial state singularities which dominate these subprocesses at low values of $p_T(\gamma^*)$. Although the total contributions from the $O(\alpha_s^2)$ subprocesses are large, they do not have a dramatic effect on the decay lepton distribution (see Figs. 1 and 2), i.e., the polarization of the virtual photon as a function of its transverse momentum is almost unchanged by higher order corrections.

We want to point out that direct measurements of the coefficients A_i for virtual photon production in pion-
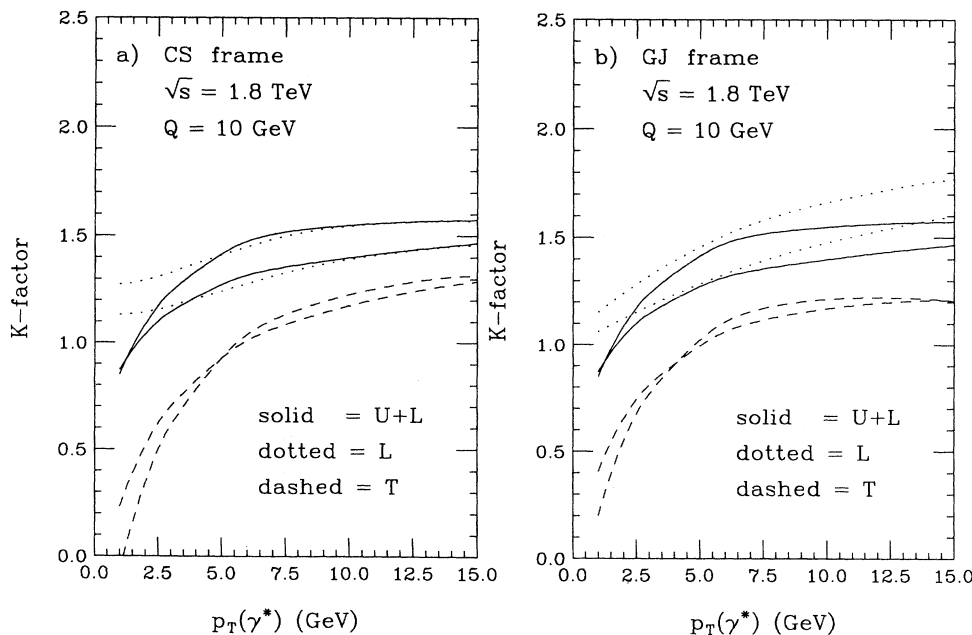

FIG. 3. K factors for the helicity cross sections $d\sigma^{U+L}$, $d\sigma^L$, and $d\sigma^T$ for $\bar{\gamma}^*$ production and decay as a function of the transverse momentum $p_T(\gamma^*)$ for $Q = 10$ GeV and $\sqrt{S} = 1.8$ TeV. Parts (a) and (b) are for the CS and GJ frames, respectively. Results are shown for two different choices of the scale $\mu^2 = \mu_F^2 = \mu_R^2$: the upper lines are for $\mu^2 = 1/4\,[p_T^2(\gamma^*) + Q^2]$ and the lower lines are for $\mu^2 = 4\,[p_T^2(\gamma^*) + Q^2]$.

nucleon scattering at $\sqrt{S} \approx 19$ and 23 GeV are not in agreement with the LO QCD predictions [1,2]. The NLO corrections to the coefficients are very small in this case (see Fig. 7 in Ref. [7]) and the results in Refs. [1] and [2] cannot be explained by standard Drell-Yan production supplemented with QCD corrections.

We now turn our attention to the $\cos\theta$ and ϕ distributions of the decay leptons. Since the effects of the NLO corrections are small (in particular for the $\cos\theta$ distribution in the CS frame; see the coefficients A_0 and α in Fig. 1), it is sufficient to use LO matrix elements in

our Monte Carlo study of the lepton decay distributions. Results will be shown for the ϕ and $\cos\theta$ distributions of leptons originating from the decay of a virtual photon produced with finite transverse momentum in $p\bar{p}$ collisions at the Tevatron center of mass energy. To demonstrate the effects of cuts, results are shown first without cuts and then with typical acceptance cuts imposed on the leptons. These cuts are necessary due to the finite acceptance of the detector.

Measurement uncertainties, due to the finite energy resolution of the detector, have been simulated in our
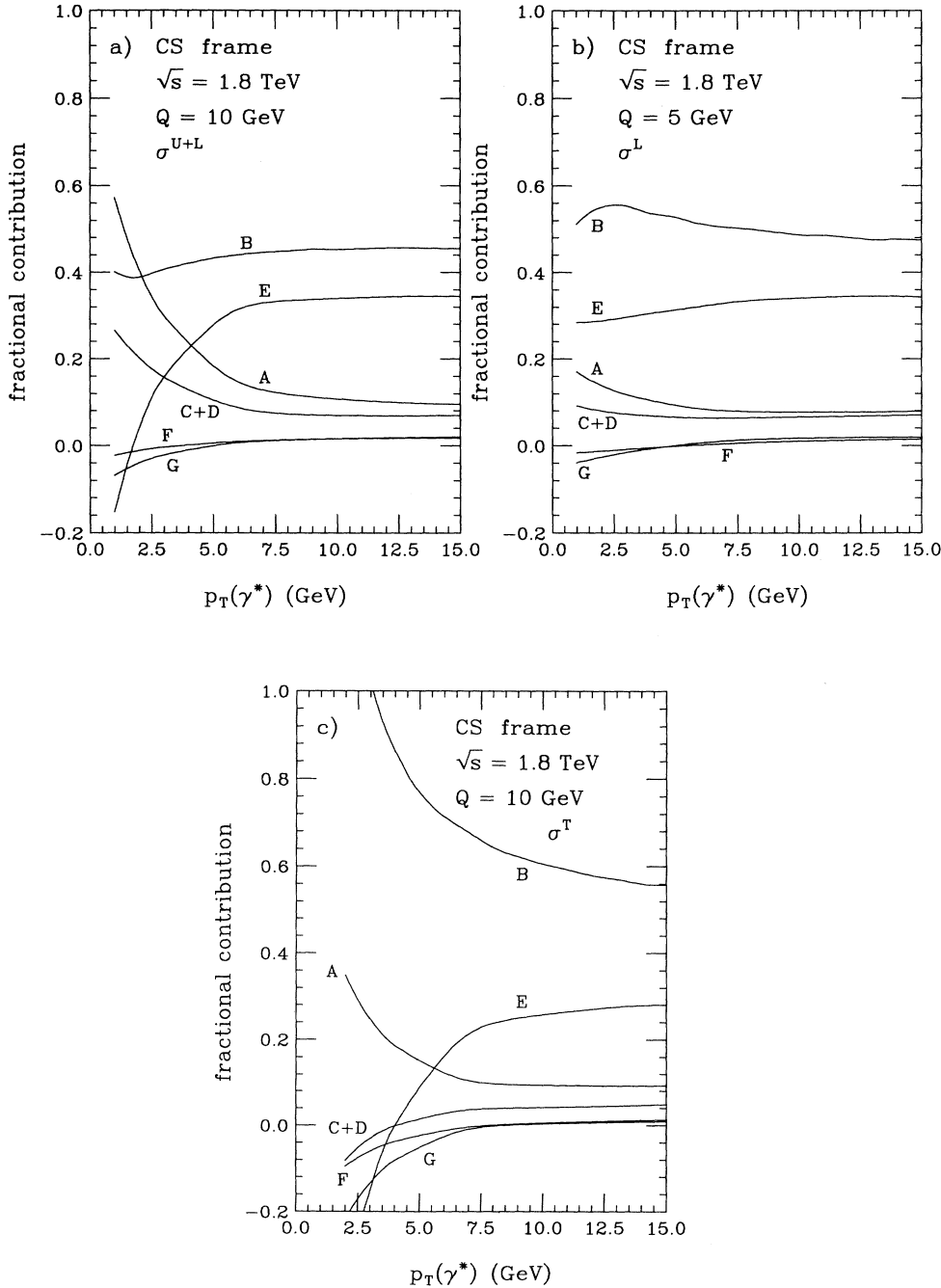

FIG. 4. (a) Fractional contributions to $d\sigma^{U+L}$ for γ^* production in the CS frame as a function of the transverse momentum $p_T(\gamma^*)$ for $Q = 10$ GeV, $\sqrt{S} = 1.8$ TeV, and $\mu^2 = 1/2\,[p_T^2(\gamma^*) + Q^2]$. The curves are labeled according to the contributing subprocesses. The LO subprocesses are (A) $q\bar{q} \rightarrow \gamma^* g$ and (B) $qg \rightarrow \gamma^* q$. The NLO subprocesses are (C+D) $(q\bar{q} \rightarrow \gamma^* g) + (q\bar{q} \rightarrow \gamma^* gg) + (q\bar{q} \rightarrow \gamma^* q\bar{q})$, (E) $(qg \rightarrow \gamma^* q) + (qg \rightarrow \gamma^* qg)$, (F) $qq \rightarrow \gamma^* qq$, (G) $gg \rightarrow \gamma^* q\bar{q}$. (b) Same as (a) but for $d\sigma^L$. (c) Same as (a) but for $d\sigma^T$.
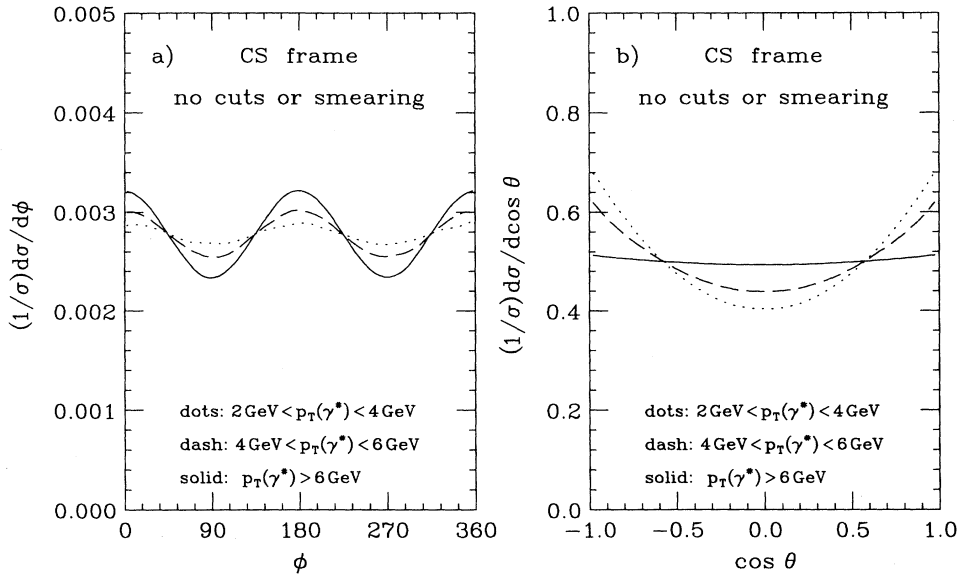
FIG. 5. (a) Normalized ϕ and (b) normalized $\cos\theta$ distributions of the leptons from γ^* decay in the CS frame with 10 GeV $<$ Q $<$ 12 GeV. Results are shown for three bins in $p_T(\gamma^*)$: 2 GeV $<$ $p_T(\gamma^*)$ $<$ 4 GeV (dotted), 4 GeV $<$ $p_T(\gamma^*)$ $<$ 6 GeV (dashed), $p_T(\gamma^*)$ $>$ 6 GeV (solid). No cuts or smearing have been applied to the decay leptons.

calculation by Gaussian smearing of the lepton four-momentum vectors with standard deviation σ. The numerical results presented here were made using σ values based on the specifications of the Collider Detector at Fermilab (CDF) Collaboration [16]. The energy resolution smearing has a negligible effect on the ϕ and $\cos\theta$ distributions.

Figure 5 shows the normalized ϕ and $\cos\theta$ distributions of the decay leptons from γ^* production for three bins in the transverse momentum of the virtual photon. The invariant mass of the photon has been integrated over the range 10 GeV $<$ Q $<$ 12 GeV. No cuts or smearing have been applied to the results in the figure. The curves in Fig. 5 can be obtained from α and β in Fig. 1(b). (Note, however, that Fig. 1 shows the coefficients α and β for a fixed value of Q = 10 GeV.) For example, since β is

an increasing function of $p_T(\gamma^*)$, the amplitude of the ϕ distribution increases with $p_T(\gamma^*)$. Likewise, α is a decreasing function of $p_T(\gamma^*)$, starting out positive and ending up negative, thus the curvature of the $\cos\theta$ distribution in Fig. 5(b) is positive for the two lowest $p_T(\gamma^*)$ bins and is nearly zero for the $p_T(\gamma^*)$ $>$ 6 GeV bin. Note that if the virtual photon was to decay isotropically, the ϕ and $\cos\theta$ distributions would both be flat.

The effect of acceptance cuts on the angular distributions is illustrated in Fig. 6 which shows the ϕ and $\cos\theta$ distributions of the decay leptons for the same bins in $p_T(\gamma^*)$ as in Fig. 5, but now with energy resolution smearing and the cuts

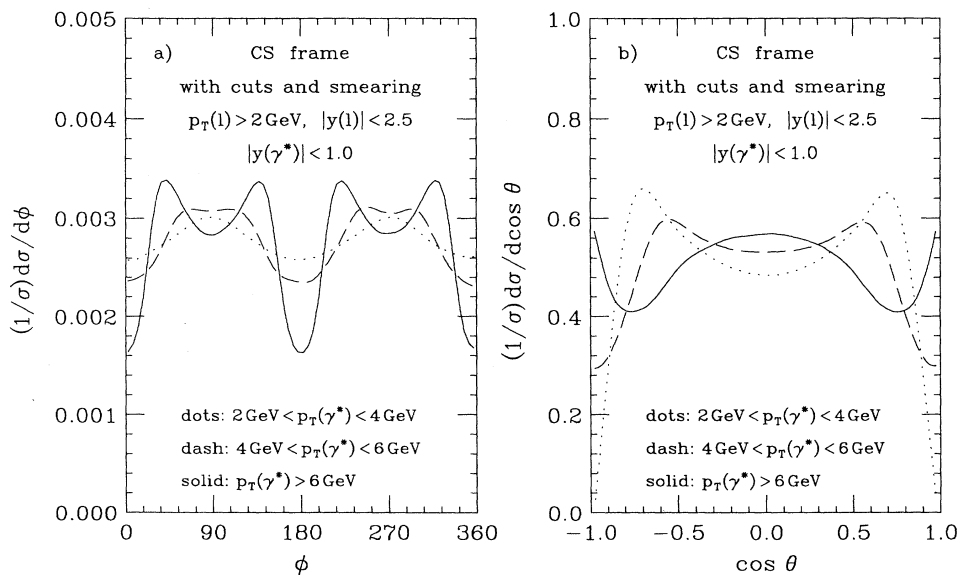$$p_T(\ell) > 2 \text{ GeV}, \quad |y(\ell)| < 2.5, \quad |y(\gamma^*)| < 1.0. \quad (40)$$

FIG. 6. Same as Fig. 5 but with smearing and the cuts $p_T(\ell)$ $>$ 2 GeV, $|y(\ell)|$ $<$ 2.5, and $|y(\gamma^*)|$ $<$ 1.0.

The cuts on the leptons are necessary due to the finite acceptance of the detector. The photon rapidity cut has been imposed because we find that polarization effects are highlighted when the virtual photon is in the central rapidity region. The cuts on the leptons, in particular the $p_T(\ell)$ cut, have a dramatic effect on the shapes of the angular distributions. The shapes of the distributions are now governed by the kinematics of the surviving events. Only 20% of the events pass these cuts. The cuts in Eq. (40), which are applied in the laboratory frame, introduce a strong ϕ dependence. The "kinematical" ϕ distribution in Fig. 6(a) is very different from the "dynamical" ϕ distribution in Fig. 5(a), in fact, the peaks and valleys are interchanged in the two distributions. The only remaining vestiges of the polarization effects in the ϕ distribution are the dips in the high $p_T(\gamma^*)$ curve (solid line) at $\phi = 90°$ and $270°$. The $\cos\theta$ distributions with cuts in Fig. 6(b) are also different from the corresponding results without cuts in Fig. 5(b), in particular for $|\cos\theta| \gtrsim 0.5$. However, for $|\cos\theta| < 0.5$ and small $p_T(\gamma^*)$ [dotted and dashed curves in Fig. 6(b)] the polarization effects in the $\cos\theta$ distributions are still visible. As stated earlier, the effect of energy resolution smearing is negligible; the drastic changes in the shapes of the distributions are due to the cuts, especially the $p_T(\ell)$ cut. The polarization effects diminish as the invariant mass of the virtual photon decreases. The LO cross section (summed over $\ell = e, \mu$) for the three $p_T(\gamma^*)$ bins, 2 GeV $< p_T(\gamma^*) < 4$ GeV, 4 GeV $< p_T(\gamma^*) < 6$ GeV, $p_T(\gamma^*) > 6$ GeV, are 50 pb, 20 pb, 26 pb, respectively. However, these numbers should be multiplied by the K factor for σ^{U+L} as shown in Fig. 3. Furthermore, soft gluon resummation effects will also be important for the production cross section at low $p_T(\gamma^*)$.

The cuts in Eq. (40) are actually quite weak. Figure 7 shows the ϕ and $\cos\theta$ distributions with the stronger and more realistic cuts

$$p_T(\ell) > 5 \text{ GeV}, \quad |y(\ell)| < 1.0, \quad |y(\gamma^*)| < 1.0, \quad (41)$$

for the same three $p_T(\gamma^*)$ bins as in Fig. 5. The curves are now very different from the curves in Fig. 5, and no traces of polarization effects are left in Fig. 7.

We have also analyzed the effect of the cuts by using the correct matrix element for γ^* production, but with isotropic decay of the virtual photon, i.e., neglecting spin correlations between γ^* production and decay. The angular distributions in this case are similar to the ones shown in Figs. 6 and 7 for the full matrix element; the remnant polarization effects discussed in Fig. 6 are of course absent.

In Fig. 8 we show ratios of the ϕ and $\cos\theta$ distributions for the same bins in $p_T(\gamma^*)$ as in Fig. 5; the distribution with full polarization has been divided by the corresponding distribution obtained with isotropic decay of the virtual photon. Cuts and smearing are included in both cases. The large effects from the cuts are expected to almost cancel in this ratio. In fact, we nearly recover the ϕ and $\cos\theta$ dependence of Fig. 5 which contains no cuts.

Figure 9 shows the ratio of the ϕ and $\cos\theta$ distributions with full polarization to the corresponding distributions obtained with isotropic leptonic decay for the virtual photon for the cuts in Eq. (41) for the high $p_T(\gamma^*)$ bin, i.e., $p_T(\gamma^*) > 6$ GeV. The kinematical effects in the two low $p_T(\gamma^*)$ bins are very large, and the cuts remove all events around $\phi = 0°, 180°, 360°$ as well as for large $\cos\theta$ values (see Fig. 7); thus it is impractical to form ratios for the two low $p_T(\gamma^*)$ bins. However, the ratios for $p_T(\gamma^*) > 6$ GeV (see Fig. 9) once again contain most of the polarization dependence seen in the solid curves of Fig. 5. The additional dips in the ϕ distribution at $\phi = 0°, 180°$, and $360°$ in Fig. 9(a) are due to the kinematical cuts. Thus even in the presence of large acceptance cuts it may be possible to highlight the polarization effects in the experimental results by dividing the experimental distributions by the corresponding Monte Carlo distributions obtained using isotropic γ^* decay.
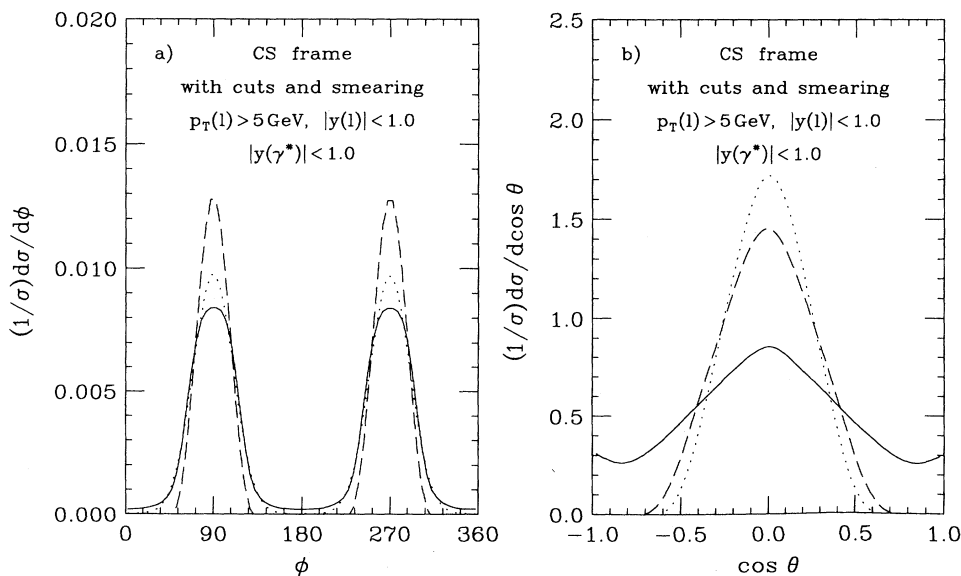

FIG. 7. Same as Fig. 5 but with smearing and the cuts $p_T(\ell) > 5$ GeV, $|y(\ell)| < 1.0$, and $|y(\gamma^*)| < 1.0$.
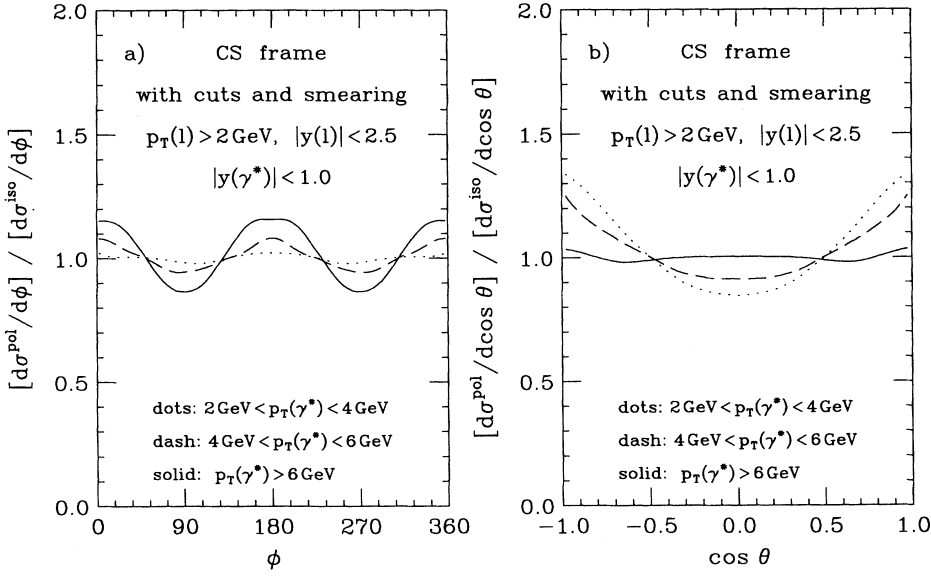
FIG. 8. Ratios of distributions in the CS frame obtained with full polarization to those obtained with isotropic decay of the γ^* for the same $p_T(\gamma^*)$ bins as in Fig. 5. Parts (a) and (b) are the ratios for the ϕ and $\cos\theta$ distributions, respectively. Energy resolution smearing and the cuts $p_T(\ell) > 2$ GeV, $|y(\ell)| < 2.5$, and $|y(\gamma^*)| < 1.0$ are included.

IV. SUMMARY

The polar and azimuthal angular distributions of the lepton pair arising from the decay of a virtual photon produced at high transverse momentum in hadronic collisions have been discussed. In the absence of cuts on the final state leptons, the general structure of the lepton angular distribution in the virtual-photon rest frame is determined by the polarization of the virtual photon. In perturbative QCD, the structure is described by four helicity cross sections, which are functions of the transverse momentum and rapidity of the virtual photon. We have calculated to $O(\alpha_s^2)$ the angular coefficients which govern the lepton angular distributions and find that the corrections are relatively small in both the CS and GJ frames, especially in the CS frame. This is because the

angular coefficients A_i are ratios of helicity cross sections and the large QCD corrections in the individual helicity cross sections tend to cancel in the ratios.

We have also studied the angular distributions of the leptonic decay products of a high p_T virtual photon when acceptance cuts and energy resolution smearing are applied to the leptons. When acceptance cuts are imposed on the leptons, the shapes of the lepton angular distributions are dominated by kinematic effects and the residual dynamical effects from the virtual photon polarization are small. The kinematic effects become more dominant as the cuts become more stringent and as the invariant mass of the photon decreases. Energy resolution smearing has a negligible effect on the angular distributions.

Polarization effects can be maximized by minimizing the cuts on the decay leptons; however, this strategy is
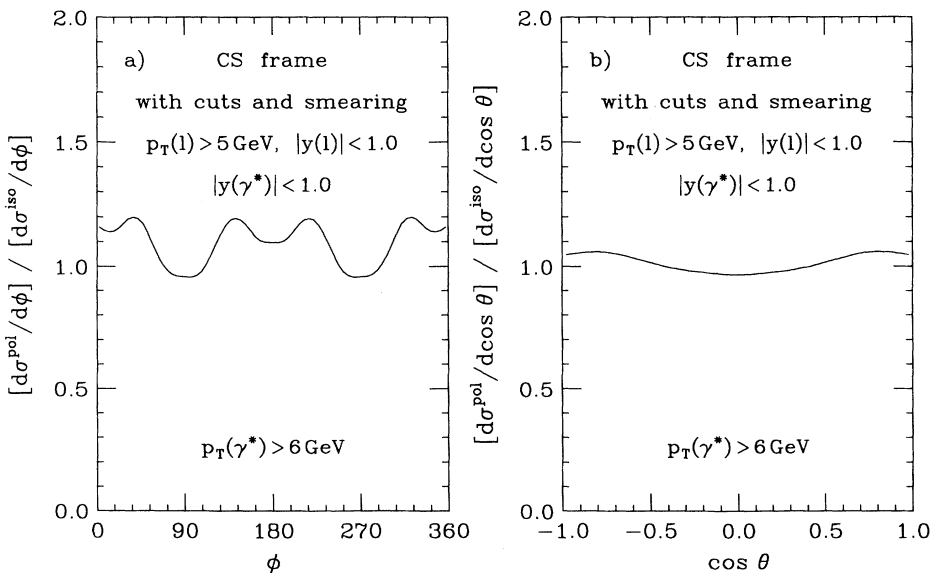

FIG. 9. Same as Fig. 8 but with the cuts $p_T(\ell) > 5$ GeV, $|y(\ell)| < 1.0$, and $|y(\gamma^*)| < 1.0$. Only the bin for $p_T(\gamma^*) > 6$ GeV is shown.

severely limited since cuts are needed due to the finite acceptance of a detector. Polarization effects are also more pronounced when the virtual photon is in the central rapidity region. Alternatively, it may be possible to highlight virtual photon polarization effects by "dividing out" the kinematic effects; i.e., if the histogrammed data are divided by the theoretical result for isotropic virtual photon decay, the resulting ratio is more sensitive to polarization effects.

ACKNOWLEDGMENTS

We thank J. G. Körner and G. A. Schuler for their advice in the NLO part of this calculation. Helpful discussions with O. Nachtmann, M. I. Martin, and D. Wood are gratefully acknowledged. This work was supported in

APPENDIX: NLO MATRIX ELEMENTS

In this appendix, we present the remaining NLO matrix elements which do not contribute to W boson production and are thus not listed in Ref. [9]. It is convenient to calculate covariant projection cross sections $d\hat{\sigma}^\beta$ [$\beta \in \{U+L, L_1, L_2, L_{12}\}$] from which one can deduce the helicity cross sections $d\hat{\sigma}^\alpha$ [$\alpha \in \{U+L, L, T, I\}$] in Eqs. (25)–(27) for any given γ^* rest frame by a transformation matrix $(M)_{\alpha\beta}$. For the CS frame one has [9]

$$
\begin{pmatrix} d\hat{\sigma}^{U+L} \\ d\hat{\sigma}^L \\ d\hat{\sigma}^T \\ d\hat{\sigma}^I \end{pmatrix}_{\text{CS}} = \begin{pmatrix} 1 & 0 & 0 & 0 \\ 0 & \frac{1}{4\cos^2\gamma_{\text{CS}}} & \frac{1}{4\cos^2\gamma_{\text{CS}}} & \frac{-1}{4\cos^2\gamma_{\text{CS}}} \\ \frac{1}{2} & -\frac{(1+\cos^2\gamma_{\text{CS}})}{8\sin^2\gamma_{\text{CS}}\cos^2\gamma_{\text{CS}}} & -\frac{(1+\cos^2\gamma_{\text{CS}})}{8\sin^2\gamma_{\text{CS}}\cos^2\gamma_{\text{CS}}} & \frac{(1-3\cos^2\gamma_{\text{CS}})}{8\sin^2\gamma_{\text{CS}}\cos^2\gamma_{\text{CS}}} \\ 0 & \frac{1}{4\sqrt{2}\sin\gamma_{\text{CS}}\cos\gamma_{\text{CS}}} & \frac{-1}{4\sqrt{2}\sin\gamma_{\text{CS}}\cos\gamma_{\text{CS}}} & 0 \end{pmatrix} \begin{pmatrix} d\hat{\sigma}^{U+L} \\ d\hat{\sigma}^{L_1} \\ d\hat{\sigma}^{L_2} \\ d\hat{\sigma}^{L_{12}} \end{pmatrix}, \tag{A1}
$$

where

$$
\cos\gamma_{\text{CS}} = \sqrt{\frac{Q^2 s}{(t-Q^2)(u-Q^2)}}, \qquad \sin\gamma_{\text{CS}} = -\sqrt{1-\cos^2\gamma_{\text{CS}}}. \tag{A2}
$$

The results for the GJ frame can be obtained from

$$
\begin{pmatrix} d\hat{\sigma}^{U+L} \\ d\hat{\sigma}^L \\ d\hat{\sigma}^T \\ d\hat{\sigma}^I \end{pmatrix}_{\text{GJ}} = \begin{pmatrix} 1 & 0 & 0 & 0 \\ 0 & 1 & 0 & 0 \\ \frac{1}{2} & -\frac{(1+\cos^2\gamma_{\text{GJ}})}{2\sin^2\gamma_{\text{GJ}}} & -\frac{1}{\sin^2\gamma_{\text{GJ}}} & \frac{\cos\gamma_{\text{GJ}}}{\sin^2\gamma_{\text{GJ}}} \\ 0 & \frac{-\cos\gamma_{\text{GJ}}}{\sqrt{2}\sin\gamma_{\text{GJ}}} & 0 & \frac{1}{2\sqrt{2}\sin\gamma_{\text{GJ}}} \end{pmatrix} \begin{pmatrix} d\hat{\sigma}^{U+L} \\ d\hat{\sigma}^{L_1} \\ d\hat{\sigma}^{L_2} \\ d\hat{\sigma}^{L_{12}} \end{pmatrix} \tag{A3}
$$

and

$$
\cos\gamma_{\text{GJ}} = 1 - \frac{2Q^2 s}{(t-Q^2)(u-Q^2)}, \qquad \sin\gamma_{\text{GJ}} = -\sqrt{1-\cos^2\gamma_{\text{GJ}}}. \tag{A4}
$$

All of the partonic projection matrix elements T^β_{ab} are listed in Ref. [9]; however, there are some interference contributions which do not contribute to W boson production because of charge conservation. The analytical results for these additional partonic projection matrix elements are listed here.

1. Diagrams $2(F_5 + F_6)^*(F_7 + F_8)$ for $q\bar{q} \rightarrow \gamma^* q\bar{q}$

The diagrams are shown in Fig. 8 of Ref. [9]. The result for the interference of these diagrams differs for vector-vector (relevant for γ^* production) and axial-axial (relevant for Z boson production) couplings. They do not contribute to W boson production. The vector-vector coupling contribution for the projection matrix elements $T^\beta_{q\bar{q}}$ for these diagrams are denoted by $D^\beta_{cd VV}$. All quantities in the following formulas are defined in Appendix F of Ref. [9]:

$$D_{cd\,VV}^{U+L}(s,t,u,Q^2) = \left(\frac{1}{2}\right)\left\langle \frac{s(s_2^2 - ut)}{ut}d_t d_u - \frac{u+t}{2ut} - (s+s_2-Q^2)\frac{(u-t)^2}{2ut\lambda^2}\right.$$

$$+\frac{f_\lambda}{\lambda}\left[(3s+2s_2)\frac{u+t}{2ut} + 2(s-Q^2)d_s - s(u+t)\frac{(u-t)^2}{2ut\lambda^2}\right]$$

$$-f_{tu}Q^2\frac{d_u d_t}{ut}(2(s_2-t)^2 + s_2^2 + s^2)$$

$$-f_{\lambda t}\frac{d_s d_u}{t}\left[(s_2-Q^2)^2 + (s_2-t)^2 + s_2^2 + s^2\right]$$

$$\left.+f_{st}\frac{d_{st}d_s}{ut}(2Q^2-t)(t^2 + 2(s_2^2 + s^2 - s_2 t))\right\rangle + \left(\frac{1}{2}\right)\langle u\leftrightarrow t\rangle,$$

$$D_{cd\,VV}^{L_1}(s,t,u,Q^2) = \left(\frac{1}{2}\right)\left\langle \frac{d_{su}}{8u}\left\{ H_1^{(1,0)}\, ud_{st}d_s\left[-48s^4 + 8s^3(13s_2 - 7t - 4u)\right.\right.\right.$$

$$-4s^2(3s_2(8s_2 - 9t) - 13u(s_2 - t) - 2u^2 + 5t^2)$$

$$-2s(2u(20s_2^2 - 27s_2 t + 8t^2) - (18s_2^2 - 21s_2 t + 4t^2)(2s_2 - t) - (9s_2 - 8t)u^2)$$

$$\left.-(5u - 8s_2 + 3t)(s_2 - u)(s_2 - t)(u - 4s_2 + 3t)\right]$$

$$+ H_1^{(1,0)}\left[4s^2(u + 3t - 2s_2) + 2s(7s_2(u - t) + 3(t^2 - u^2) - 2(s_2^2 - ut))\right.$$

$$\left.+(2s_2 - u - t)(7(s_2 - u)^2 - (s_2 - t)^2)\right]$$

$$+ H_1^{(1,1)}\,(s_2 - u)\left[2(s(u - 2s_2) + 2(2s_2 - u - t)(s_2 - u))\right.$$

$$\left.+d_{st}u(4s^2 - 2s(u + t - s_2) + (s_2 - u)(u + s_2 - 2t))\right]$$

$$+ H_1^{(1,2)}\,(s_2 - u)^2\left[(2s_2 - u - t) + ud_s d_{st}(-4s^2 - 2s(3u - 4s_2 + t)\right.$$

$$\left.+(s_2 - t)(3u - 4s_2 + t))\right] + H_1^{(1,3)}\,ud_{st}(s_2 - u)^3$$

$$+ H_2^{(1,1)}\,2(s_2 - t)\left[(4s_2 - 2u - 3t)s - (s_2 - t)(2s_2 - u - t)\right.$$

$$\left.+\frac{ud_{st}}{2}\left(16s^2 + 2s(3u - 11s_2 + 7t) + 2u(u - 7s_2) + t(10u + t - 12s_2) + 13s_2^2\right)\right]$$

$$+ H_2^{(1,2)}\,(s_2 - t)^2\left[-(2s_2 - u - t) + ud_{st}d_s(-12s^2 - 2s(5u - 12s_2 + 7t)\right.$$

$$\left.-(3u - 4s_2 + t)(u - 3s_2 + 2t))\right] + H_2^{(1,3)}\,u(s_2 - t)^3 d_{st}$$

$$+ 2d_t\left[4s^2 s_2 + 2s(s_2(2u - 3t - s_2) + 2t^2)\right.$$

$$\left.-(s_2 - t)((t - s_2)^2 - 3(u - s_2)^2)\right] + d_{st}\frac{2u}{3}(24s^2 - 4s(4s_2 - 3t)$$

$$\left.\left.+(u - t)^2 + 16(s_2 - u)(s_2 - t))\right\}\right.$$

$$-\frac{1}{2u}\left\{f_{tu}2d_{su}d_{st}((s_2 - u)(s_2 - t) - ss_2)(s - u + s_2)\right.$$

$$+ f_{su}us(s - u + s_2)d_s d_{st} - f_{\lambda u}d_{su}(s - u + s_2)(s_2 - u + d_s us)$$

$$- f_{st}d_{su}s(u - s - s_2 + d_s u(s_2 - u - 3s))$$

$$\left.\left.+ f_{\lambda t}d_s d_{st}u((Q^2 - s_2)(s_2 - t) - s^2)\right\}\right\rangle,$$

$$D_{cd\,VV}^{L_2}(s,t,u,Q^2) = D_{cd\,VV}^{L_1}(s,u,t,Q^2),$$

$$D_{cd\,VV}^{L_{12}}(s,t,u,Q^2) = \left(\frac{1}{2}\right)\left\langle \frac{-d_{su}d_{st}}{8ut}\left\{ -H_1^{(1,0)}\, d_s\left[8s^4(3u^2-5ut-6us_2)\right.\right.\right.$$

$$+4s^3(4u^2(3u-2t)-13us_2(3u-t)+30us_2^2)$$

$$+2s^2(2u^3(8u+9t)-u^2(73us_2+22t^2)+5u^2s_2(9t+20s_2)-12us_2^2(4t+3s_2))$$

$$+s(3u^4(3u+t)-4u^3(13us_2+19t^2)$$

$$+12u^2ts_2(17t+8u)+8u^2s_2^2(11u-52t)-4us_2^3(7u-49t+6s_2))$$

$$+u^5(u+2t-7s_2)-3u^4(9t^2-4s_2^2)+5u^3ts_2(5u+46t)+10u^2s_2^3(u-4s_2)$$

$$\left.+8us_2^4(3s_2-14t)+2u^2ts_2^2(179s_2-129t-93u)-32u^3t^3\right]$$

$$+H_1^{(1,1)}\,2(s_2-u)\left[3s^2u(u-3t-2s_2)+(s4u^2(u-3s_2)\right.$$

$$-3ut(u+t-4s_2)+4s_2^2(2u-t)+2t^2s_2)+u^3(u+t-4s_2)$$

$$\left.+2ut(2s_2-u)(4t-3s_2)-3t^2(ut+2s_2^2)+us_2^2(5u-2s_2)+2ts_2(t^2+2s_2^2)\right]$$

$$-H_1^{(1,2)}\,d_s(s_2-u)^2\left[2s^2(u(u-8t-2s_2)-t(t-2s_2))\right.$$

$$+s(3(u^3-t^3)+10s_2(t^2-u^2)+8s_2(4ut+us_2-ts_2)-ut(17u+15t))$$

$$+5s_2(t^3-u^3)+u^2(u^2+9ts_2+8s_2^2)-t^2(t^2+6ut-23us_2+10u^2)$$

$$\left.-4us_2^2(s_2+4t)+4ts_2^2(s_2-2t)\right]$$

$$-H_1^{(1,3)}\,2ut(s_2-u)^3-4s^2\left[u(3t-2u+s_2)+2s_2^2-ss_2\right]$$

$$+\frac{2}{3}s\left[3u^2(t+5u)-6s_2(6t^2-s_2^2)+22s_2ut\right]-\frac{2}{3}u^2t(17t-47s_2)$$

$$\left.-2u^3(3s_2-u)-\frac{4}{3}u\left(14ts_2^2-3s_2^3+tu^2\right)\right\}$$

$$+\frac{d_{st}}{2ut}\{f_{tu}d_{su}\left[s(Q^2-s_2-2s)+s_2(Q^2-s)-2ut\right]\left[(s_2-u)(s_2-t)-ss_2\right]$$

$$+f_{su}sd_s\left[2s^2(u-2s_2)+s(u(u+5t)-2s_2(u+2t))\right.$$

$$\left.-4s_2^2(Q^2-s)-ut(2u-t-3s_2)+u^2s_2\right]$$

$$\left.\left.+f_{\lambda t}d_{su}\left[ss_2(2s_2-u-t)+stu+(s_2-t)(2t-s_2)(t+u-2s_2)\right]\right\}\right\rangle$$

$$+\left(\frac{1}{2}\right)\left\langle u\leftrightarrow t\right\rangle.$$

2. Diagrams $2(H_1+H_2)^*(H_3+H_4)$ and $2(H_5+H_6)^*(H_7+H_8)$ for $qq\to\gamma^*qq$

The diagrams are shown in Fig. 9 of Ref. [9]. The vector-vector coupling contribution for the projection matrix elements T_{qq}^β for the diagrams $2(H_1+H_2)^*(H_3+H_4)$ and $2(H_5+H_6)^*(H_7+H_8)$ are denoted by $E_{ab\,VV}^\beta$ and $E_{cd\,VV}^\beta$, respectively, and can be obtained from the matrix elements $D_{cd\,VV}^\beta$ listed above:

$$E_{ab\,VV}^\beta(s,t,u,Q^2) = E_{cd\,VV}^\beta(s,u,t,Q^2) = -D_{cd\,VV}^\beta(s,u,t,Q^2).$$

[1] NA10 Collaboration, S. Falciano *et al.*, Z. Phys. C **31**, 513 (1986); NA10 Collaboration, M. Guanziroli *et al.*, *ibid.* **37**, 545 (1988).

[2] J.S. Conway *et al.*, Phys. Rev. D **39**, 92 (1989); J.G. Heinrich *et al.*, *ibid.* **44**, 44 (1991).

[3] S.D. Drell and T.M. Yan, Phys. Rev. Lett. **25**, 316 (1970).

[4] For reviews and further references see, e.g., J.C. Collins, D.E. Soper, and G. Sterman, Nucl. Phys. **B261**, 104 (1985); **B308**, 833 (1988); G. Sterman, Phys. Lett. B **179**, 281 (1986); Nucl. Phys. **B281**, 310 (1987); J.C. Collins and D.E. Soper, Annu. Rev. Nucl. Part. Sci. **37**, 383 (1987); T. Matsuura and W.L. van Neerven, Z. Phys. C **38**, 623 (1988); J.C. Collins, D.E. Soper, and

G. Sterman, in *Factorization of Hard Processes in Perturbative QCD*, edited by A.H. Mueller (World Scientific, Singapore, 1990); G.T. Bodwin, Phys. Rev. D **31**, 2616 (1985); G.T. Bodwin, S.J. Brodsky, and G.P. Lepage, *ibid.* **39**, 3287 (1989).

[5] O. Nachtmann and A. Reiter, Z. Phys. C **24**, 283 (1984); J. Ellis, M.K. Gaillard, and W.J. Zakrzewski, Phys. Lett. **81B**, 224 (1979).

[6] O. Nachtmann, University of Heidelberg Report No. HD-THEP-94-42, 1994 (unpublished).

[7] A. Brandenburg, O. Nachtmann, and E. Mirkes, Z. Phys. C **60**, 697 (1993).

[8] A. Brandenburg, S.J. Brodsky, V.V. Khoze, and D. Müller, Phys. Rev. Lett. **73**, 939 (1994).

[9] E. Mirkes, Nucl. Phys. **B387**, 3 (1992).

[10] J.C. Collins and D.E. Soper, Phys. Rev. D **16**, 2219 (1977).

[11] E. Mirkes and J. Ohnemus, Phys. Rev. D **50**, 5692 (1994).

[12] W.A. Bardeen, A.J. Buras, D.W. Duke, and T. Muta, Phys. Rev. D **18**, 3998 (1978).

[13] K. Gottfried and J.D. Jackson, Nuovo Cimento **33**, 309 (1964).

[14] A.D. Martin, R.G. Roberts, and W.J. Stirling, Phys. Rev. D **50**, 6734 (1994).

[15] C.S. Lam and W.-K. Tung, Phys. Rev. D **18**, 2447 (1978); **21**, 2712 (1980); Phys. Lett. **80B**, 228 (1979); K. Kajantie, J. Lindfors, and R. Raitio, *ibid.* **74B**, 384 (1978); Nucl. Phys. **B144**, 422 (1978); J. Cleymans and M. Kuroda, Phys. Lett. **80B**, 385 (1979); Nucl. Phys. **B155**, 480 (1979); R.L. Thews, Phys. Rev. Lett. **43**, 987 (1979); J. Lindfors, Phys. Scr. **20**, 19 (1979); R.J. Oakes, Nuovo Cimento **44A**, 440 (1966).

[16] CDF Collaboration, F. Abe *et al.*, Phys. Rev. D **45**, 3921 (1992).